# Phonon-phonon interactions in the polarization dependence of Raman scattering

Nimrod Benshalom, <sup>1,\*</sup> Maor Asher, <sup>1,\*</sup> Rémy Jouclas, <sup>2</sup> Roman Korobko, <sup>1</sup> Guillaume Schweicher, <sup>2</sup> Jie Liu, <sup>2</sup> Yves Geerts, <sup>2,3</sup> Olle Hellman, <sup>4,5,†</sup> and Omer Yaffe<sup>1,‡</sup>

<sup>1</sup>Department of Chemical and Biological Physics,
Weizmann Institute of Science, Rehovot 76100, Israel

<sup>2</sup>Laboratoire de Chimie des Polymères, Université Libre de Bruxelles (ULB), 1050 Brussels, Belgium

<sup>3</sup>International Solvay Institutes for Physics and Chemistry, 1050 Brussels, Belgium

<sup>4</sup>Department of Physics, Chemistry and Biology (IFM),
Linköping University, SE-581 83, Linköping, Sweden

<sup>5</sup>Department of Molecular Chemistry and Material Science,
Weizmann Institute of Science, Rehovot 76100, Israel
(Dated: June 23, 2023)

We have found that the polarization dependence of Raman scattering in organic crystals at finite temperatures can only be described by a fourth-rank tensor formalism. This generalization of the second-rank Raman tensor  $\mathcal{R}$  stems from the effect of off-diagonal components in the crystal self-energy on the light scattering mechanism. We thus establish a novel manifestation of phonon-phonon interaction in inelastic light scattering, markedly separate from the better-known phonon lifetime.

The Raman spectrum of crystals is usually interpreted through the prism of mode assignment, where each spectral peak is assigned an irreducible representation (irrep) of the relevant space group [1]. So entrenched was this perspective, that past studies would denote their measurement geometry in terms of the irreps observable by it [2–8]. This conceptual framework, also known as factor group analysis, provides a rigorous tool-set to connect observed spectra with crystal structure and vibrational symmetries. Besides predicting the number of Raman active modes and their degeneracy, factor group analysis also dictates the polarization dependence of a spectral feature associated with a specific irrep. The connection between the polarization of incident and scattered light is thus governed by the assigned irrep. Most textbooks [9– 14], as well as contemporary research [15–18], use the matrix representation, also known as the Raman tensor, to describe this irrep-specific polarization dependence. In this matrix formalism the scattering cross-section of a Raman peak, assigned an irrep  $\Gamma_x$  and corresponding Raman tensor  $\mathcal{R}_{\Gamma_x}$ , is determined by [9]

$$\sigma_{\Gamma_x} \propto |\hat{\boldsymbol{e}}_i \cdot \mathcal{R}_{\Gamma_x} \cdot \hat{\boldsymbol{e}}_s|^2,$$
 (1)

where  $\hat{e}_i$  and  $\hat{e}_s$  are the incident, and collected light polarization unit vectors, respectively. This expression completely governs the polarization dependence of the Raman signal, with the angle entering through the geometrical relationship between the polarization unit vectors and crystal orientation (see Fig. 1a). The components of  $\mathcal{R}_{\Gamma_x}$  are contracted susceptibility derivatives evaluated at equilibrium, so along with its persistent irrep identification Eq. (1) predicts a temperature independent polarization pattern.

However, some of us recently showed the polarizationorientation (PO) Raman response, i.e., the polarization dependence of the Raman signal, evolves with temperature for some organic crystals [19, 20]. These kind of PO patterns and their temperature dependence can not be captured by any superposition of irrep specific matrices and a generalization to a fourth-rank formalism is necessary. We argue this is the result of specific phononphonon interactions entering the Raman scattering process, an effect which is highly temperature and material dependent. To further elucidate the physical origins of the effect, we adopt a generalized many-body treatment of the Raman scattering cross-section. We find that by allowing off-diagonal components in the self-energy to persist, different irrep contributions in the spectrum are mixed, and a fourth-rank formalism is engendered. Because the magnitude of these components is expected to be temperature dependent, this accounts for both the observed PO pattern and its temperature evolution. We confirm the validity of the model by successfully fitting it to experimental spectra.

This inadequacy of Eq. (1) stems from the naïve treatment of temperature dependence in its derivation, which implicitly assumes a constant parabolic potential surface for atomic displacements, also known as the harmonic approximation [9, 21]. The role of anharmonicity in solid-state Raman spectroscopy has been the subject of extensive study, not only from an analytical point of view [22–24], but also from computational [25–27], and experimental [28–32] perspectives. However, despite the consensus over the prominence of anharmonicity in Raman scattering, its effect on polarization has not been considered before Asher et al. [19].

We apply our generalized model on the PO spectra of a few organic crystals, focusing on [1]benzothieno[3,2-b]benzothiophene (BTBT) as an ideal showcase. As promising organic semiconducting molecular crystals, BTBT and its derivatives have been intensively investigated due to their high mobility and other application-

<sup>\*</sup> These authors contributed equally

<sup>†</sup> olle.hellman@weizmann.ac.il

<sup>†</sup> omer.yaffe@weizmann.ac.il

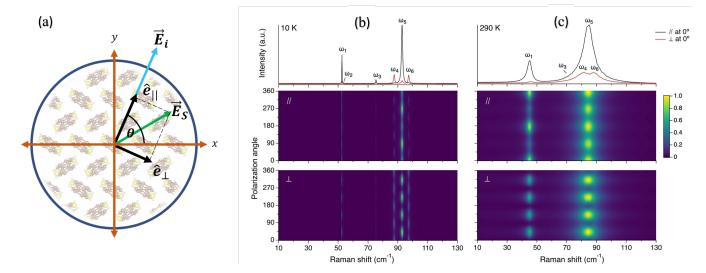


FIG. 1. (a) Face-on schematic of a PO measurement. (b) PO measurement of BTBT at 10 K. (c) PO measurement of BTBT at 290 K. An example spectrum ( $\theta = 0^{\circ}$ ) for each configuration is given (top panels). Parallel measurement probes the scattered field's projection on  $\hat{e}_{\parallel}$  (middle panels), and cross measurement probes the scattered field's projection on  $\hat{e}_{\perp}$  (bottom panels).

oriented properties, such as air-stability and solution processability [33–38]. Besides its scientific importance, BTBT proved especially suitable for this study as its separate spectral features display the different possible PO trends with temperature, showing that the need for a fourth-rank formalism is not only material and temperature dependent, but may also be mode specific.

Our experimental setup employed a back-scattering geometry, as shown in Fig. 1a. In a PO measurement the polarization of the incident laser beam  $(E_i)$  is rotated in a plane parallel to the BTBT (001) crystal face. The inelastically back-scattered light can generally assume any polarization  $(E_s)$ . We separately probe the projection of scattered light onto either a parallel  $(\hat{e}_{\parallel})$  or cross  $(\hat{e}_{\perp})$  polarization with respect to the incident beam. Full details for the measurement procedure and sample characterization are given in sections SI-II in the Supporting Information [39–43].

Fig. 1b and c present the Stokes Raman PO data for BTBT measured at 10 K and 290 K, respectively. At 10 K we observe exactly six sharp peaks, as predicted by Raman selection rules (Sec. SIX.1 in the Supporting Information [44]). At 290 K we observe five distinguishable peaks, due to the low intensity of  $\omega_2$  and the broadness of the spectrum. The correspondence between spectral peaks across temperatures is corroborated by continuously sampling the Raman spectrum throughout the temperature range (Sec. SVI in the Supporting Information). The polarization angle (vertical axis) in figures 1b and c is off-set by a random angle controlled by the crystal orientation in the laboratory frame, but is consistent for all spectra.

To examine the PO dependence of each spectral feature we must first extract its integrated intensity. We do this by fitting the raw spectra to a sum of six Lorentzians,

in agreement with factor group analysis, and then extract the integrated intensity of each separate peak (see Sec. SIII in the Supporting Information). Because we are only interested in the polarization dependence, other deconvolution procedures may be chosen. We perform this process for the PO measurements at 10 K, 80 K, 150 K, 220 K, and 290 K (see sections SVII and SVIII in Supporting Information for the raw data and extracted temperature dependent PO pattern of each spectral feature, respectively). With the PO pattern at hand, we can apply our model of choice to interpret it.

Figure 2a presents the temperature evolution of the PO pattern for peak  $\omega_4$  extracted from Fig. 1, *i.e.*, the change with temperature of the polarization dependence of its integrated intensity. The PO pattern is highly temperature dependent in both parallel and cross configurations (see Sec. SIV in Supporting Information for the temperature independent PO response of silicon [45]). This temperature dependence in BTBT is fully reversible upon cooling, ruling out static disorder as its origin.

Following the harmonic approximation, we apply Eq. (1) and determine the appropriate irrep  $\Gamma_x$  and its corresponding Raman matrix  $\mathcal{R}_{\Gamma_x}$ . We account for birefringence effects by using a corrected Raman tensor, introducing a relative phase factor between the diagonal tensor components of  $\mathcal{R}_{\Gamma_x}$  [17]. For our alternative, temperature dependent treatment, we follow Cowley [46] and Born and Huang [47] before him, who described the Raman cross-section with a fourth-rank tensor

$$\sigma(\Omega) \propto \sum_{\mu\nu\xi\rho} n_{\mu} n_{\xi} I_{\mu\nu\xi\rho}(\Omega) E_{\nu} E_{\rho}, \tag{2}$$

where  $\Omega$  is the probing frequency,  $\boldsymbol{E}$  is the incident electric field and  $\boldsymbol{n}$  is the unit vector for the observed polarization, with Greek letters standing for Cartesian

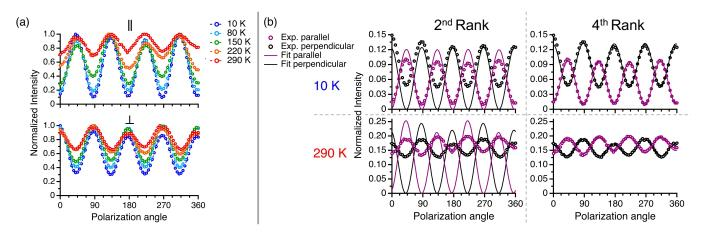


FIG. 2. (a) The PO Raman response of  $\omega_4$  from 10-290 K in parallel (top panel) and cross (bottom panel) configurations. (b) The fit results of the PO Raman response of  $\omega_4$  at 10 K (top panels) and 290 K (bottom panels) using the second-rank (left panels), and fourth-rank Raman tensor formalism (right panels).

components. Because the Raman matrix in Eq. (1) is squared, casting it into a fourth-ranked tensor is immediately valid. However, its necessity compared to the prevalent second-rank formalism has never been demonstrated experimentally, nor was it considered theoretically. We discuss the physical justification for Eq. (2) below, but for now treat  $I_{\mu\nu\xi\rho}$  phenomenologically as the general material property governing light scattering in the crystal. The tensor structure and component ratios of  $I_{\mu\nu\xi\rho}$  will determine the PO pattern observed in experiment. Unlike Eq. (1) this generalized form has the potential of producing non-negative values, but this is irrelevant when fitting experimental data to Eq. (2). We discusses the positive semi-definiteness of the scattering tensor in sec. SIX.5 in the Supporting Information [48–50].

Fig. 2b shows the fitting attempts using both the predicted irrep (left panels), and generalized fourth-rank tensor (right panels), for the same  $\omega_4$  spectral feature at 10 K and 290 K (see sections SIX.2-3 in Supporting Information for all fitting tensors and results [9, 17, 19, 51]). Using the harmonic Raman tensor, we find a partial fit at 10 K, which gradually deteriorates as temperature increases up to room temperature. In stark contrast, the fourth-rank tensor formalism gives a near perfect fit for all data sets. A general fourth-rank tensor obviously offers a much larger parameter space, but symmetry considerations dramatically reduce the number of independent variables in  $I_{\mu\nu\xi\rho}$ . We thus find the correct observable material property governing the Raman scattering around  $\omega_4$  is a fourth-rank tensor. Similar behavior was previously observed in the Raman spectra of anthracene and pentacene crystals [19], where again, the appropriate fourth-rank tensor faithfully reproduces all PO patterns (see Sec. SX in the Supporting Information [19]).

The matrix  $\mathcal{R}$  used in Fig. 2b is the specific irrep appropriate one. However, even a completely unconstrained second-rank tensor, with an additional phase parameter for birefringence effects [17], was not able to successfully

fit Eq. (1). Importantly, in our experiment this generalized form for  $\mathcal{R}$  has more parameters than the symmetry reduced form of  $I_{\mu\nu\xi\rho}$  (five vs. four). The different PO patterns made possible by each formalism depend on the measuring geometry, but one concrete example is demonstrated in Fig. 2; in our back-scattering setup, any symmetric second-rank tensor will make the cross signal vanish with 4-fold periodicity. Indeed, this prohibits a successful fit to many of the observed spectra. Conversely, the fourth-rank tensor has no such limitation, allowing a faithful reproduction of the measured PO patterns.

We rationalize the use of a fourth-rank tensor by considering the inelastic light scattering mechanism of anharmonic crystals. Assuming only dipole scattering, the inelastic light scattering of a crystal as a function of probing frequency  $\Omega$  is governed by [46]

$$I_{\mu\nu\xi\rho}(\Omega,T) = \frac{1}{2\pi} \int \left\langle \chi_{\mu\nu}^*(t) \, \chi_{\xi\rho}(0) \right\rangle_T e^{-i\Omega t} dt, \quad (3)$$

the Fourier transform of the thermally averaged susceptibility auto-correlation function at temperature T. The presentation here and full derivation in Sec. SXI of the Supporting Information use Hartee atomic units [21, 27, 52–58]. The fundamental physical entity - susceptibility  $(\chi)$ , is indeed a second-rank tensor operator, but since experimentally we measure intensity, the observable is defined by the tensor product of two susceptibilities operators.

Using normal mode coordinates  $A_{qs}$  for mode s with momentum q, and expanding the susceptibility in atomic displacements to first order, Eq. (3) transforms to [59]

$$I_{\mu\nu\xi\rho} = \sum_{\lambda,\lambda'} \chi_{\lambda'}^{*\mu\nu} \chi_{\lambda'}^{\xi\rho} \int \langle A_{\lambda}(t) A_{\lambda'}(0) \rangle_T e^{-i\Omega t} dt, \quad (4)$$

where we adopted a composite index  $\lambda$  to denote qs, and  $\chi_{\lambda}^{\mu\nu}$  are the susceptibility derivatives with respect to normal-mode displacement  $\lambda$ . The thermal average

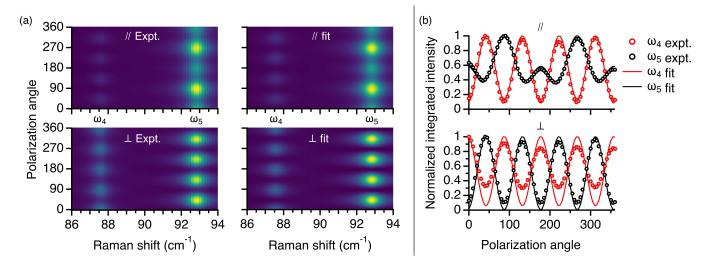


FIG. 3. Global fit of the two-mode model for the PO patterns of spectral features  $\omega_4$  and  $\omega_5$  in the Raman spectra of BTBT. (a) Measurement (left) and fit (right) for parallel (top) and cross (bottom) configurations. (b) The integrated intensity of each feature as extracted from measurement (circles) and fit (lines).

 $\langle \cdots \rangle_T$  in Eq. (4) is taken over crystal configurations. Except for the susceptibility derivatives, previously discussed by some of us [27], the problem has reduced to one of lattice dynamics.

The ionic motion inside a crystal can be solved with the single-particle Green's function [56]

$$G_{\lambda\lambda'}(\Omega, T) = -i \int \theta(t) \langle [A_{\lambda}(\tau), A_{\lambda'}(0)] \rangle_T e^{-i\Omega t} dt, \quad (5)$$

where  $\theta(t)$  is the Heaviside step function. It is commonly written as a sum of the harmonic Green's function  $g_{\lambda\lambda'}^0$  and a complex self-energy term  $\Sigma_{\lambda\lambda'}(\Omega)$ :

$$G(\Omega)^{-1} = g^0(\Omega)^{-1} + \Sigma(\Omega). \tag{6}$$

We can make Eq. (4) more analytically transparent by using the corresponding spectral function [56],

$$J_{\lambda\lambda'}(\Omega, T) = -\frac{1}{\pi} \operatorname{Im} \left\{ G_{\lambda\lambda'} \right\}. \tag{7}$$

The generalized anharmonic scattering tensor becomes

$$I(\Omega, T)_{\mu\nu\xi\rho} = \sum_{\lambda\lambda'} \chi^{*\mu\nu}_{\lambda} \chi^{\xi\rho}_{\lambda'} \left[ n(\Omega, T) + 1 \right] J_{\lambda\lambda'}(\Omega), \quad (8)$$

where  $n(\Omega, T)$  is the Bose-Einstein occupation number for energy  $\hbar\Omega$  at temperature T.

To demonstrate how phonon-phonon interactions lead to a fourth-rank tensor description, we evaluate Eq. (8) for the simplest case of two "mixed" normal modes with different irreps. The derivatives  $\chi^{\mu\nu}_{\lambda'}$  are the same as in the harmonic treatment, so the Raman selection rules remain valid. The BTBT structure only allows for  $A_g$  and  $B_g$  Raman active modes [44]. However, these selection rules do not prohibit multiple terms contributing into the same frequency interval. Retaining all Raman

active modes will yield an intractable expression, so we consider the mixing of two modes with different irreps. Absorbing the diagonal self-energy real part into the resonance frequencies  $\omega_s$ , our harmonic Green's function and self-energy term become [56]

$$g^{0}(\Omega) = \begin{pmatrix} \frac{2\omega_{A_{g}}}{\Omega^{2} - \omega_{A_{g}}^{2}} & 0\\ 0 & \frac{2\omega_{B_{g}}}{\Omega^{2} - \omega_{B_{g}}^{2}} \end{pmatrix}; \quad \Sigma = \begin{pmatrix} i\Gamma_{A_{g}} & \gamma\\ \gamma & i\Gamma_{B_{g}} \end{pmatrix},$$

$$(9)$$

where we assumed real off-diagonal self-energy components  $\gamma$ , originally introduced by Barker and Hopfield to explain the infrared reflectivity of perovskites [60], later used to explain their Raman spectra [61, 62], but hitherto ignored in vector (polarization) analysis. Importantly, these past studies invoked  $\gamma$  to explain spectral line-shapes, and are therefore open to competing diagonal self-energy descriptions. Because our PO measurements probe the tensor structure of the scattering mechanism, we are able to exclude a diagonal model and thus demonstrate the unique signature of off-diagonal self-energy components. Generally, the self-energy is also frequency dependent,  $\Sigma = \Sigma(\Omega)$ , but since the fitted spectral features are relatively sharp (3 cm<sup>-1</sup>), we assume a constant. The full spectral function, (Eq. S11), is given in Sec. SXI.4 in the Supporting Information.

The mixed derivative terms  $\chi_{A_g}^* \otimes \chi_{B_g}$  vanish due to symmetry considerations. Explicitly rewriting the tensorial part of Eq. (8) for our two-mode model, we obtain

$$I(\Omega,T) \propto \chi_{\mathrm{A_g}}^* \otimes \chi_{\mathrm{A_g}} J_{\mathrm{A_gA_g}} + \chi_{\mathrm{B_g}}^* \otimes \chi_{\mathrm{B_g}} J_{\mathrm{B_gB_g}}.$$
 (10)

It would appear that we have recovered a quasi-harmonic expression, with each term corresponding to a separate spectral feature. However, the off-diagonal component  $\gamma$  dramatically changes the frequency dependence of the

spectral functions  $J(\Omega)$ . Instead of a single Lorentzianlike feature centered around a single resonance frequency, they now each have appreciable contributions in both  $\omega_{A_g}$ and  $\omega_{B_g}$ . It is impossible to re-create the tensorial structure of Eq. (10) by squaring a single matrix (Eq. (1)), and a fourth-rank tensor formalism must be invoked.

Another way to understand the unique effect of the offdiagonal components is to examine the temperature dependence of the phonon's eigenvectors. Whereas diagonal self-energy components modify the phonon's lifetime and resonance frequency (*i.e.*, eigenvalue), the off-diagonal components change the eigenvector, or identity, of the vibrational mode. We can parameterize the linear combination describing the re-normalized eigenvectors using the self-energy term. If the temperature-dependent spectral function is diagonalized by

$$\mathbb{J}(T) = Q^{-1}J(T)Q,\tag{11}$$

then the temperature dependent eigenvector  $v_i(T)$  is given by

$$\boldsymbol{v}_i(T) = \sum_{j} \left( Q^{\mathrm{T}} \right)_{ij} \boldsymbol{v}_j^0, \tag{12}$$

where the index j sums over all the zero-temperature (harmonic) eigenvectors  $v_j^0$  within the coupled subspace (two in our case), and the dimensionality of  $v_i$  is determined, as usual, by the number of atoms in the unit cell.

The model described by equations (2) and (10) is tested by performing a global fit to the measured spectral range around  $\omega_5$  (A<sub>g</sub>) and  $\omega_4$  (B<sub>g</sub>) in BTBT (Fig. 2). Besides their appropriate irreps, our choice of peaks is guided by the PO pattern of  $\omega_4$  that defies Eq. (1), and by their spectral proximity, predicted to increase the effect of mixing between the spectral functions (see Eq. (S11) in Sec. SIX.4 in Supporting Information).

The spectra for a full set of PO measurements (parallel and cross) at a given temperature  $(T=10\ K)$  are fitted simultaneously to the two-mode model. All fit functions, parameters and procedure are given in Sec. SIX.4 in the Supporting Information. Fig. 3a presents the zoomed-in PO measurement at 10 K alongside the fit results for the same frequency range. The integrated intensity of each feature in each configuration was extracted from the fit and compared to the experimental values in Fig. 3b. We find the parallel signal (top) matches the fit perfectly, with the cross (bottom) showing a slightly exaggerated oscillation amplitude, especially for  $\omega_4$ .

The global fit uses five parameters for all spectra, and is therefore not as accommodating as the fully general fourth-rank tensor used in Fig. 2, where the PO of each peak is fitted to four independent parameters. The pertinent comparison, however, is to the original harmonic model of Eq. (1). Even when fully relaxing symmetry constraints and allowing for birefringence (totaling in seven independent parameters), Eq. (1) gave an inferior fit compared to the two-mode model. We emphasize that although all equations are strictly rigorous, substantial simplifying approximations were introduced into the

model. Our choice to mix "only" two modes, as well as the choice of which two, is not uniquely prescribed by any physical principle, so we do not expect Eq. (10) to fit the PO spectra perfectly. Furthermore, using a constant self-energy is at odds with the fully general frequency-dependent expression (Eq. S29 in the Sec. SXI.2 in the Supporting Information [27, 52–55]). We argue, however, that this approximated model is the minimally generalized treatment capable to explain the observed PO patterns and their temperature evolution. Appreciable contributions from off-diagonal self-energy components is therefore a necessary qualification of any full description of Raman scattering in these systems.

The spectra and fits for another peak,  $\omega_1$ , are presented in Fig. 4. Unlike the PO patterns of  $\omega_4$ , fitting Eq. (1) to  $\omega_1$  proved satisfactory for all temperatures, with the generalized fourth-rank tensor offering only a modest improvement (Fig. 4b). Importantly, the PO pattern of  $\omega_1$  still exhibits a clear evolution with temperature (Fig. 4a), which can not be explained by harmonic theory.

These two different scenarios demonstrate an important distinction in our interpretation of the mode mixing described by the self-energy off-diagonal components. If an irrep-specific second-rank tensor is able to capture the PO pattern, then same-irrep couplings have primarily contributed to the peak. Because the anharmonic spectral function is temperature dependent, the weight of each contributing mode can change with temperature, altering the PO response. Alternatively, whenever we observe a departure from the 4-fold cross pattern described above, a fourth-rank tensor must be invoked, and mixing between different irreps must be the culprit. We can therefore immediately determine spectral feature  $\omega_4$  (Fig. 2) arises from appreciable  $\langle A_q, B_q \rangle$  interactions, even without the benefit of an explicit fit. This statement can potentially be tested further by numerical simulations [26], or a 2D-Raman measurement [63], where inter-mode correlations are directly evaluated.

Note that examination of any single BTBT spectrum would not hint at any extraordinary anharmonic effects, as the spectral features themselves are not particularly broad, nor do they display exceptional softening upon heating. The significance of off-diagonal components is therefore not necessarily correlated with the overall magnitude of the self-energy term. Indeed, it is perhaps the relative conventional spectrum shape that made the observation possible.

The two-mode model presented above allowed for a finite correlation between vibrational modes with different irreps. Strictly speaking, these should vanish out of symmetry considerations [64]. This apparent contradiction is resolved by the fact that Raman scattering does not probe true  $\Gamma$ -point phonons. Momentum conservation in the scattering process confers some finite momentum q to the vibrational excitation, determined by the measurement geometry and crystal orientation. Both participating  $\Gamma$ -irreps map into identical irreps of G(q), the group of the wave-vector, so their coupling is allowed [64]. In

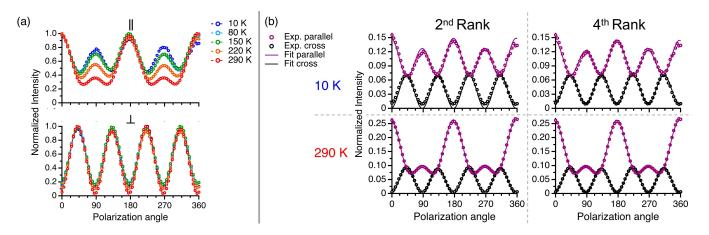


FIG. 4. (a) The PO Raman response of  $\omega_1$  from 10-290 K in parallel (top panel) and cross (bottom panel) configurations. (b) The fit results of the PO Raman response of  $\omega_1$  at 10 K (top panels) and 290 K (bottom panels) using the second-rank Raman tensor formalism (left panels) and the fourth-rank Raman tensor formalism (right panels).

other words, the Green's function remains invariant under the symmetry operations of the q-vector and therefore need not vanish. In this sense, our use of the  $\Gamma$ -point susceptibility derivatives  $\chi_{\Gamma}$  is an approximation, retrospectively justified by the successful global fit.

Finally, another possible generalization of the analysis presented is to consider light scattering from non-vibrational crystal excitations. The distinction between the underlying dipole radiation mechanism, given in terms of a second-rank tensor, and the actual observable intensity, given in terms of a fourth-rank tensor, is completely general. Considering the symmetry constrained fourth-rank tensor as the fundamental material property might benefit other spectroscopic scenarios, such as exciton or magnon scattering.

In conclusion, we have demonstrated the unique role of anharmonicity in the polarization dependence of inelastic light scattering at finite temperatures. We showed that the observed PO patterns of BTBT and other organic crystals can only be explained by generalizing the tensor structure governing Raman scattering to fourthrank. This generalization is theoretically justified by allowing off-diagonal self-energy components to persist, which represents the mixing between vibrational modes and re-normalization of their eigenvectors.

The proposed fourth-rank model was realized by a sum of susceptibility tensor products with *different* irreducible representations, and successfully tested by performing a global fit to the PO response of adjacent spectral features.

It is desirable to predict which vibrational modes will couple, as well as understand the temperature evolution of the off-diagonal self-energy components that describe them. Perturbative methods offer a recipe for their calculation, given a known potential surface [53, 56, 65], but mapping chemical structure to such a surface is a formidable task in and of itself. Generally, the effect is expected to depend on the whole of the vibrational dispersion relation, and require methods that provide the effective temperature dependent potential surface [27, 66], to fully understand.

#### ACKNOWLEDGEMENTS

O. Y. Acknowledges funding from the European Research Counsel (850041 - ANHARMONIC). Support from the Swedish Research Council (VR) program 2020-04630 is gratefully acknowledged. Y. G. is thankful to the Belgian National Fund for Scientific Research (FNRS) for financial support through research projects Pi-Fast (No T.0072.18), Pi-Chir (No T.0094.22), DIFFRA (No U.G001.19), 2D to 3D (No O.005018F), and CHISUB (No O.00322). Financial supports from the French Community of Belgian (ARC no 20061) is also acknowledged. G. S. is a research associate of the FNRS.

Hayes, W.; Loudon, R. Scattering of Light by Crystals;
 Dover Books on Physics; Dover Publications: Mineola,
 NY. 1978; p 368.

<sup>[2]</sup> Ganguly, B. N.; Kirby, R. D.; Klein, M. V.; Montgomery, G. P. Raman-Active Resonance Modes, Overtones, and Anharmonicity in NaCl:Cu+. *Physical Review Letters* 1972, 28, 307–309.

<sup>[3]</sup> Güntherodt, G.; Grünberg, P.; Anastassakis, E.; Cardona, M.; Hackfort, H.; Zinn, W. Phonons in GdS-Raman scattering of an fcc metal. *Physical Review B* 1977, 16, 3504–3512.

<sup>[4]</sup> Montgomery, G. P.; Klein, M. V.; Ganguly, B. N.; Wood, R. F. Raman Scattering and Far-Infrared Absorption Induced by Silver Ions in Sodium Chloride. *Physical* 

- Review B 1972, 6, 4047–4060.
- [5] Potts, J. E.; Walker, C. T.; Nair, I. R. Temperature dependence of second-order raman scattering in potassium and rubidium halides. *Physical Review B* 1973, 8, 2756– 2771.
- [6] Haberkorn, R.; Buchanan, M.; Bilz, H. Evidence for intra-ionic anharmonicity in the Raman spectra of cubic ionic crystals. Solid State Communications 1973, 12, 681–683.
- [7] Buchanan, M.; Bauhofer, W.; Martin, T. P. Impurityinduced Raman scattering in CsBr and CsI. *Physical Re*view B 1974, 10, 4358–4363.
- [8] Ishigame, M.; Yoshida, E. Study of the defect-induced Raman spectra in cubic zirconia. Solid State Ionics 1987, 23, 211–218.
- [9] Yu, P. Y.; Cardona, M. Springer; Graduate Texts in Physics; Springer Berlin Heidelberg: Berlin, Heidelberg, 2010; Vol. 1.
- [10] Long, D. A. The Raman effect: a unified treatment of the theory of Raman scattering by molecules; John Wiley & Sons Ltd, p 597.
- [11] Loudon, R. Advances in Physics; 1964; Vol. 13; pp 423–482.
- [12] Pinczuk, A.; Burstein, E. In Light Scattering in Solids; Cardona, M., Ed.; Topics in Applied Physics; Springer Berlin Heidelberg: Berlin, Heidelberg, 1975; Vol. 8; pp 23–78.
- [13] Weber, W.; Merlin, R. In Materials Science; Weber, W. H., Merlin, R., Eds.; Springer Series in Materials Science 9; Springer Berlin Heidelberg: Berlin, Heidelberg, 2000; Vol. 42; p 492.
- [14] Dresselhaus, M. S.; Dresselhaus, G.; Jorio, A. Springer; Springer-Verlag Berlin and Heidelberg GmbH & Co.: Berlin, Heidelberg, 2008; p 582.
- [15] Livneh, T.; Zhang, J.; Cheng, G.; Moskovits, M. Polarized Raman scattering from single GaN nanowires. *Physical Review B - Condensed Matter and Materials Physics* 2006, 74.
- [16] Sander, T.; Eisermann, S.; Meyer, B. K.; Klar, P. J. Raman tensor elements of wurtzite ZnO. *Physical Review B* 2012, 85, 165208.
- [17] Kranert, C.; Sturm, C.; Schmidt-Grund, R.; Grundmann, M. Raman Tensor Formalism for Optically Anisotropic Crystals. *Physical Review Letters* 2016, 116, 127401.
- [18] Sharma, R.; Menahem, M.; Dai, Z.; Gao, L.; Brenner, T. M.; Yadgarov, L.; Zhang, J.; Rakita, Y.; Korobko, R.; Pinkas, I.; Rappe, A. M.; Yaffe, O. Lattice mode symmetry analysis of the orthorhombic phase of methylammonium lead iodide using polarized Raman. *Physical Review Materials* 2020, 4, 051601.
- [19] Asher, M.; Angerer, D.; Korobko, R.; Diskin-Posner, Y.; Egger, D. A.; Yaffe, O. Anharmonic Lattice Vibrations in Small-Molecule Organic Semiconductors. Advanced Materials 2020, 32, 1908028.
- [20] Asher, M.; Jouclas, R.; Bardini, M.; Diskin-posner, Y.; Kahn, N.; Korobko, R.; Kennedy, A. R.; Moraes, L. S. D.; Schweicher, G.; Liu, J.; Beljonne, D.; Geerts, Y.; Ya, O. Chemical Modifications Suppress Anharmonic Effects in the Lattice Dynamics of Organic Semiconductors. ACS Materials Au 2022,
- [21] Dove, M. Oxford University Press, 1st ed.; Oxford University Press Inc.: New-York, 2003; p 334.

- [22] Wallis, R. F.; Maradudin, A. A. Ionic Raman Effect. II. The First-Order Ionic Raman Effect. *Physical Review B* 1971, 3, 2063–2075.
- [23] Loudon, R. Theory of the first-order Raman effect in crystals. Proceedings of the Royal Society of London. Series A. Mathematical and Physical Sciences 1963, 275, 218-232.
- [24] Cowley, R. A. Anharmonic crystals. Reports on Progress in Physics 1968, 31, 123–166.
- [25] Putrino, A.; Parrinello, M. Anharmonic Raman spectra in high-pressure ice from ab initio simulations. *Physical Review Letters* 2002, 88, 1764011–1764014.
- [26] Raimbault, N.; Athavale, V.; Rossi, M. Anharmonic effects in the low-frequency vibrational modes of aspirin and paracetamol crystals. *Physical Review Mate*rials 2019, 3, 53605.
- [27] Benshalom, N.; Reuveni, G.; Korobko, R.; Yaffe, O.; Hellman, O. Dielectric response of rock-salt crystals at finite temperatures from first principles. *Physical Review Materials* 2022, 6, 033607.
- [28] Spitzer, J.; Etchegoin, P.; Cardona, M.; Anthony, T.; Banholzer, W. Isotopic-disorder induced Raman scattering in diamond. Solid State Communications 1993, 88, 509–514.
- [29] Widulle, F.; Ruf, T.; Konuma, M.; Silier, I.; Cardona, M.; Kriegseis, W.; Ozhogin, V. I. Isotope effects in elemental semiconductors: A Raman study of silicon. *Solid State Communications* 2001, 118, 1–22.
- [30] Menéndez, J.; Cardona, M. Temperature dependence of the first-order Raman scattering by phonons in Si, Ge, and α-Sn: Anharmonic effects. *Physical Review B* 1984, 29, 2051–2059.
- [31] Mihailovic, D.; McCarty, K. F.; Ginley, D. S. Anharmonic effects and the two-particle continuum in the Raman spectra of YBa2Cu3O6.9, TlBa2CaCu2O7, and Tl2Ba2CaCu2O8. Physical Review B 1993, 47, 8910–8916.
- [32] Cardona, M.; Ruf, T. Phonon self-energies in semiconductors: anharmonic and isotopic contributions. Solid State Communications 2001, 117, 201–212.
- [33] Takimiya, K.; Ebata, H.; Sakamoto, K.; Izawa, T.; Otsubo, T.; Kunugi, Y. 2,7-Diphenyl[1]benzothieno[3,2-b]benzothiophene, a new organic semiconductor for air-stable organic field-effect transistors with mobilities up to 2.0 cm2 V-1 s-1. Journal of the American Chemical Society 2006, 128, 12604–12605.
- [34] Takimiya, K.; Osaka, I.; Mori, T.; Nakano, M. Organic semiconductors based on [1]benzothieno[3,2-B][1]benzothiophene substructure. Accounts of Chemical Research 2014, 47, 1493–1502.
- [35] Ebata, H.; Izawa, T.; Miyazaki, E.; Takimiya, K.; Ikeda, M.; Kuwabara, H.; Yui, T. Highly soluble [1]benzothieno[3,2-b]benzothiophene (BTBT) derivatives for high-performance, solution-processed organic field-effect transistors. *Journal of the American Chemical Society* 2007, 129, 15732–15733.
- [36] Schweicher, G. et al. Bulky end-capped [1]Benzothieno[3,2-b]benzothiophenes: Reaching highmobility organic semiconductors by fine tuning of the crystalline solid-state Order. Advanced Materials 2015, 27, 3066-3072.
- [37] Wawrzinek, R.; Sobus, J.; Chaudhry, M. U.; Ahmad, V.; Grosjean, A.; Clegg, J. K.; Namdas, E. B.; Lo, S. C. Mobility Evaluation of [1]Benzothieno[3,2-

- b][1]benzothiophene Derivatives: Limitation and Impact on Charge Transport. ACS Applied Materials and Interfaces **2019**, 11, 3271–3279.
- [38] Ma, Z.; Geng, H.; Wang, D.; Shuai, Z. Influence of alkyl side-chain length on the carrier mobility in organic semiconductors: Herringbone: vs. pi-pi stacking. *Journal of Materials Chemistry C* 2016, 4, 4546–4555.
- [39] Vyas, V. S.; Gutzler, R.; Nuss, J.; Kern, K.; Lotsch, B. V. Optical gap in herringbone and π-stacked crystals of [1]benzothieno[3,2-b]benzothiophene and its brominated derivative. CrystEngComm 2014, 16, 7389-7392.
- [40] Niebel, C. et al. Thienoacene dimers based on the thieno[3,2-b]thiophene moiety: Synthesis, characterization and electronic properties. *Journal of Materials* Chemistry C 2015, 3, 674–685.
- [41] Matsumura, M.; Muranaka, A.; Kurihara, R.; Kanai, M.; Yoshida, K.; Kakusawa, N.; Hashizume, D.; Uchiyama, M.; Yasuike, S. General synthesis, structure, and optical properties of benzothiophene-fused benzoheteroles containing Group 15 and 16 elements. Tetrahedron 2016, 72, 8085–8090.
- [42] Macrae, C. F.; Edgington, P. R.; McCabe, P.; Pid-cock, E.; Shields, G. P.; Taylor, R.; Towler, M.; Van De Streek, J. Mercury: Visualization and analysis of crystal structures. *Journal of Applied Crystallography* 2006, 39, 453–457.
- [43] Macrae, C. F.; Bruno, I. J.; Chisholm, J. A.; Edgington, P. R.; McCabe, P.; Pidcock, E.; Rodriguez-Monge, L.; Taylor, R.; Van De Streek, J.; Wood, P. A. Mercury CSD 2.0 New features for the visualization and investigation of crystal structures. *Journal of Applied Crystallography* 2008, 41, 466–470.
- [44] Rousseau, D. L.; Bauman, R. P.; Porto, S. P. S. Normal Mode Determination in Crystals. *Journal of Raman Spectroscopy* 1981, 10, 253–290.
- [45] Lu, Z. Q.; Quinn, T.; Reehal, H. S. Polarization-dependent Raman spectra of thin crystalline silicon films. Journal of Applied Physics 2005, 97, 033512.
- [46] Cowley, R. A. The theory of Raman scattering from crystals. *Proceedings of the Physical Society* **1964**, *84*, 281–296.
- [47] Born, M.; Huang, K. Dynamical Theory of Crystal Lattices; Clarendon Oxford: Oxford, 1954; p 432.
- [48] Nye, J.; Nye, P. Physical Properties of Crystals: Their Representation by Tensors and Matrices; Oxford science publications; Clarendon Press, 1985.
- [49] Slezák, O.; Lucianetti, A.; Mocek, T. Tensor-to-matrix mapping in elasto-optics. J. Opt. Soc. Am. B 2020, 37, 1090–1097.
- [50] van den Bos, A. Parameter Estimation for Scientists and Engineers; John Wiley & Sons, Inc.: Hoboken, NJ, USA,

- 2007; pp 259-263.
- [51] Aroyo, M. I.; Perez-Mato, J. M.; Capillas, C.; Kroumova, E.; Ivantchev, S.; Madariaga, G.; Kirov, A.; Wondratschek, H. Bilbao Crystallographic Server: I. Databases and crystallographic computing programs. Zeitschrift für Kristallographie - Crystalline Materials 2006, 221, 15-27.
- [52] Leibfried, G.; Ludwig, W. Theory of Anharmonic Effects in Crystals. Solid State Physics - Advances in Research and Applications 1961, 12, 275–444.
- [53] Cowley, R. The lattice dynamics of an anharmonic crystal. Advances in Physics 1963, 12, 421–480.
- [54] Wallace, D. C. Thermodynamics of crystals; Dover Books on Physics; Dover Publications, Incorporated, 1998.
- [55] Semwal, B. S.; Sharma, P. K. Thermal Conductivity of an Anharmonic Crystal. *Physical Review B* 1972, 5, 3909– 3014
- [56] Kwok, P. C. In Green's Function Method in Lattice Dynamics; Seitz, F., Turnbull, D., Ehrenreich, H. B. T. S. S. P., Eds.; Academic Press, 1968; Vol. 20; pp 213–303.
- [57] Maradudin, A. A.; Fein, A. E.; Vineyard, G. H. On the evaluation of phonon widths and shifts. *Physica Status* Solidi (B) 1962, 2, 1479–1492.
- [58] Fultz, B. Vibrational thermodynamics of materials. Progress in Materials Science 2010, 55, 247–352.
- [59] Hayes, W.; Loudon, R. Scattering of Light by Crystals; Dover Publications, 1978; pp 25–31.
- [60] Barker, A. S.; Hopfield, J. J. Coupled-optical-phonon-mode theory of the infrared dispersion in BaTiO3, SrTiO3, and KTaO3. Physical Review 1964, 135, A1732–A1737.
- [61] Chaves, A.; Katiyar, R. S.; Porto, S. P. Coupled modes with A1 symmetry in tetragonal BaTiO3. *Physical Review B* 1974, 10, 3522–3533.
- [62] Sanjurjo, J. A.; Katiyar, R. S.; Porto, S. P. Temperature dependence of dipolar modes in ferroelectric BaTiO3 by infrared studies. *Physical Review B* 1980, 22, 2396–2403.
- [63] Hurwitz, I.; Raanan, D.; Ren, L.; Frostig, H.; Oulevey, P.; Bruner, B. D.; Dudovich, N.; Silberberg, Y. Single beam low frequency 2D Raman spectroscopy. *Optics Express* 2020, 28, 3803.
- [64] Maradudin, A. A.; Ipatova, I. P. Structure of the Phonon Propagator for an Anharmonic Crystal. *Journal of Math*ematical Physics 1968, 9, 525–532.
- [65] Maradudin, A. A.; Fein, A. E. Scattering of Neutrons by an Anharmonic Crystal. *Physical Review* 1962, 128, 2589–2608.
- [66] Hellman, O.; Steneteg, P.; Abrikosov, I. A.; Simak, S. I. Temperature dependent effective potential method for accurate free energy calculations of solids. *Physical Review B* 2013, 87, 104111.

# Supplemental Information

# Phonon-phonon interactions in the polarization dependence of Raman scattering

Nimrod Benshalom, 1,\* Maor Asher, 1,\* Rémy Jouclas, 2 Roman Korobko, 1 Guillaume Schweicher, 2 Jie Liu², Yves Geerts, 2,3 Olle Hellman, 4,5,† and Omer Yaffe 1,‡

- <sup>1</sup>Department of Chemical and Biological Physics, Weizmann Institute of Science, Rehovot 76100, Israel.
- <sup>2</sup>Laboratoire de Chimie des Polymères, Université Libre de Bruxelles (ULB), 1050 Brussels, Belgium
  - $^3$ International Solvay Institutes for Physics and Chemistry, 1050 Brussels, Belgium
- <sup>4</sup>Department of Physics, Chemistry and Biology (IFM), Linköping University, SE-581 83, Linköping, Sweden
- <sup>5</sup>Department of Molecular Chemistry and Material Science, Weizmann Institute of Science, Rehovot 76100, Israel
- \* These authors contributed equally.
- † olle.hellman@liu.se
- ‡ omer.yaffe@weizmann.ac.il

#### SI Measurement details

Crystals Growth and characterization: [1]benzothieno[3,2-b]benzothiophene (BTBT) single-crystals were grown by leaving a saturated BTBT solution in chloroform in open air at room temperature until complete chloroform evaporation. We confirmed the crystal structure and high phase purity of the crystals by performing XRD measurements (see Sec. SII).

Temperature-Dependent PO Raman: A custom-built Raman system was used to conduct the Raman measurements. The system included a 785 nm Toptica diode laser with intensity of around 30 mW on the sample. To control the polarization of the incident and scattered light for the polarization-dependent measurements (5° steps), rotating half-wave plates and a polarizer-analyzer combination were used. The system included a 50x objective. Notch filters are included in the system to allow access to the low-frequency region (>10 cm<sup>-1</sup>) and simultaneous acquisition of the Stokes and anti-Stokes signal. The system is based on a 1 m long Horiba FHR-1000 dispersive spectrometer with a 1800 mm<sup>-1</sup> grating. The spectral resolution was approximately 0.15 cm<sup>-1</sup>. The temperature was set and controlled by a Janis cryostat ST-500 and a temperature controller by Lakeshore model 335.

#### SII Powder X-ray diffraction measurements of BTBT

Preferred orientation and phase purity of BTBT were analyzed using powder X-ray diffraction. The experiment was performed at room temperature. The Compound was finely ground using a mortar and pestle for phase confirmation measurement. Single crystals were mounted over the sample holder for preferential orientation analysis. For BTBT the measurements were conducted on a Panalytical Empyrean diffractometer using Cu–K $\alpha$  radiation ( $\lambda$  =1.54178 Å). The diffractometer was set up with reflection-transmission spinner 3.0 configuration, and patterns were collected with  $2\theta$  range between 5.0 and 30.0°, steps of 0.1°, time per step of 2.5 s, and rotation of 1 r/s. A calculated pattern was obtained from known crystal structure of BTBT [1–3] using Powder Pattern tool on Mercury software [4, 5]. The crystalline phase of BTBT was confirmed to have the same phase of the known crystal structures with CSD Refcode PODKEA02 [3] (BTBT) as it can be observed in Figure S1 (experimental diffraction pattern in red and calculated diffraction patterns in black). The results show single crystals of BTBT with highly (100) preferred orientation crystallized along [001] direction.

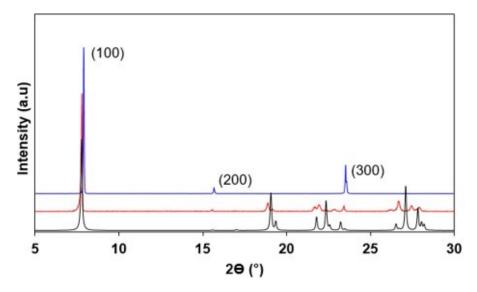


**Figure S1:** X-Ray diffraction patterns calculated from the known crystal structures (in black), obtained experimentally from powders (in red) and obtained experimentally from single crystals (in blue) of BTBT.

#### SIII Deconvolution of Raman spectra

To extract the integrated intensity of a spectral feature, we fit the measured Stokes-shift Raman spectra with the product of the Bose-Einstein distribution and a multi-damped Lorentz oscillator line shape,

$$I_{Raman}(\Omega) = \left(\frac{1}{e^{\frac{\hbar\Omega}{k_BT}} - 1} + 1\right) \sum_{i} \frac{c_i |\Omega| \Gamma_i^3}{\Omega^2 \Gamma_i^2 + (\Omega^2 - \omega_i^2)^2}$$
(S1)

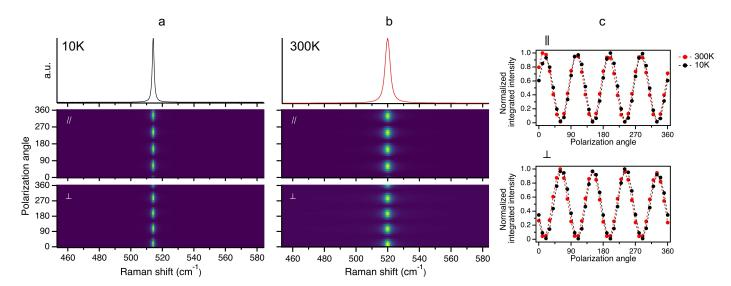
Where  $\omega_i$ ,  $c_i$  and  $\Gamma_i$  are the position, intensity, and width of each peak, respectively.  $\Omega$  is the measured frequency (Raman shift), T is the temperature,  $\hbar$  is the Planck constant and  $k_B$  is the Boltzmann constant. The Lorentz in Equation (S1) is a variation of the Lorentz oscillator, where c is the maximum value of the peak. Given the fitted Lorentzian parameters, the integrated intensity of the spectral feature is

$$I_{int} = \left[n_{\text{BE}}(\omega_i, T) + 1\right] \frac{2c_i \left|\omega_i\right| \Gamma_i^2}{\sqrt{4\omega_i^2 - \Gamma_i^2}} \left[\frac{\pi}{2} - \tan^{-1}\left(\frac{\Gamma_i^2 - 2\omega_i^2}{\Gamma_i \sqrt{4\omega_i^2 - \Gamma_i^2}}\right)\right],\tag{S2}$$

with  $n_{\rm BE}$  standing for an approximated Bose-Einstein constant pre-factor.

#### SIV The temperature independent polarization-orientation Raman of silicon

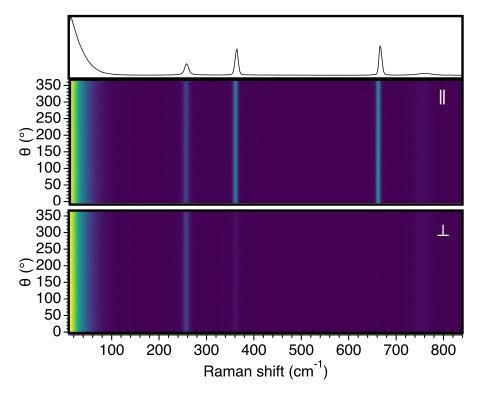
Figure S2 presents the PO Raman measurements of a (100) silicon wafer at 10 K and 300 K with the analysis of the polarization dependence of the integrated intensity of the prominent Raman peak (the TO phonon at around 520 cm<sup>-1</sup>). We performed the measurements and analysis similar to the organic crystals discussed in the main text using the same optical setup. We present these results as an example for an inorganic material that shows a temperature independent PO response, in agreement with the harmonic picture. Furthermore, according to theory, the intensity of the prominent Raman peak should go down to zero at the minimum point [6]. In our measurement, the peak intensity drops to about 1% of its maximum intensity, showing our system suffers very little leakage.



**Figure S2:** Temperature dependence of the PO Raman of silicon. (a) and (b) presents the PO Raman measurement of silicon at 10 K and 300 K, respectively. The middle and bottom panels present the measurements in parallel and cross configurations, respectively. The top panel presents the unpolarized spectrum (sum over all angles). (c) presents the polarization dependence of the integrated intensity of the prominent Raman peak. The top and bottom panels present the results for parallel and cross configurations, respectively.

#### SV Polarization-orientation Raman of chloroform

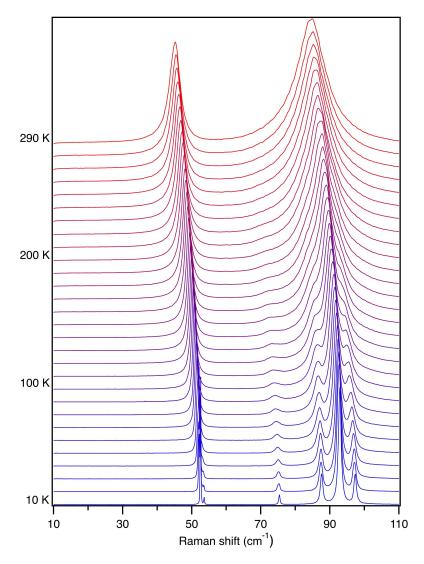
Figure S3 presents the PO Raman measurement of liquid chloroform at room temperature. The measurement was performed similarly to the organic crystals discussed in the main text using the same optical setup. Since there is no long-range order in a liquid, we expect the measurement to be polarization independent. This is why measuring the PO response of a liquid is helpful as a test for the system response to the change in polarization angle. Our results show that the PO response of the vibrations of chloroform is completely polarization-independent - proving our systems response is minimal.



**Figure S3:** Polarization dependent measurement of liquid chloroform in parallel and cross configurations. The top panel shows a typical spectrum in the parallel configuration.

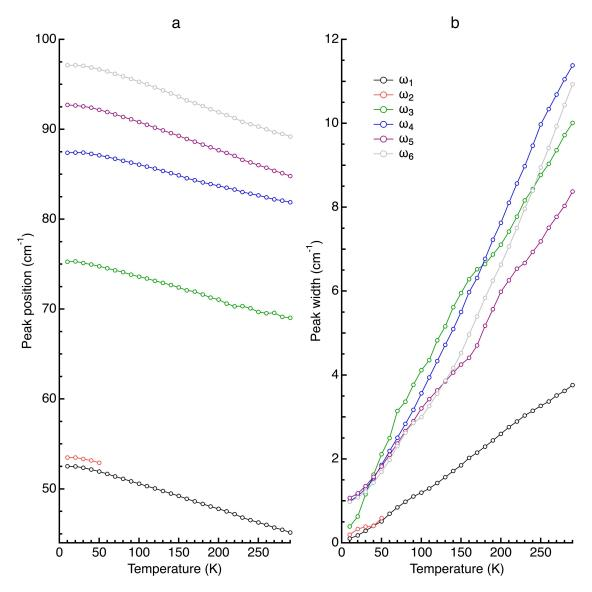
# SVI Temperature dependent low-frequency Raman spectroscopy of BTBT

Figure S4 shows the temperature dependent low-frequency Raman spectroscopy spectra of BTBT, from 10 K to 290 K at 10 K increments. We see only a gradual redshift and broadening of the spectrum as temperature increases. No abrupt changes to the Raman spectrum indicate there is no phase transition in the measured temperature range.



**Figure S4:** Temperature dependent low-frequency Raman of BTBT. The spectra were normalized and shifted up for clarity. The temperature increment is 10 K.

Figure S5 shows the temperature dependence of the peaks position and full-width-half-maximum (FWHM) of the lattice vibrations, extracted from fitting the spectra according to Sec. SIII. The trend with temperature of vibrational frequency and FWHM is primarily linear.



**Figure S5:** The temperature dependence of the vibrational frequencies (a) and FWHM (b) of the lattice vibrations of BTBT.

# SVII Raman polarization-orientation color maps of BTBT

Figure S6 presents the raw data obtained from the PO Raman measurements for both parallel and cross configurations for a single crystal of BTBT at 10, 80, 150, 200, and 290 K.

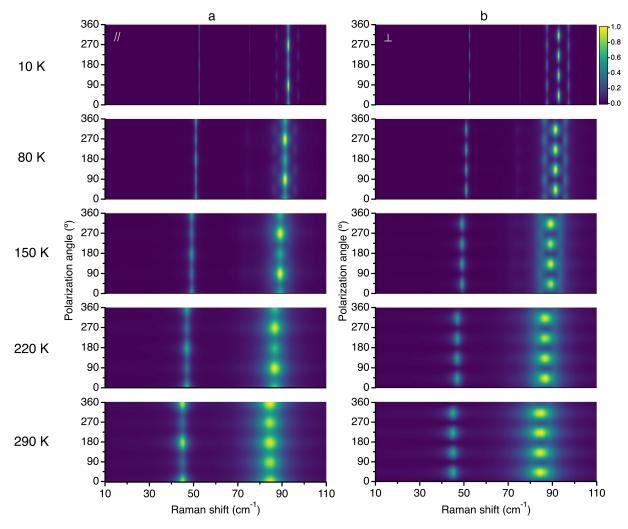


**Figure S6:** Raw PO Raman of BTBT in (a) parallel and (b) cross configurations at 10 K, 80 K, 150 K, 220 K and 290 K.

# SVIII Temperature evolution in the Raman polarization-orientation response of BTBT

Figure S7 presents the temperature evolution of the PO pattern of each separate peak in the Raman spectrum of BTBT. The results show the PO Raman response of all BTBT lattice vibrations evolves with temperature.

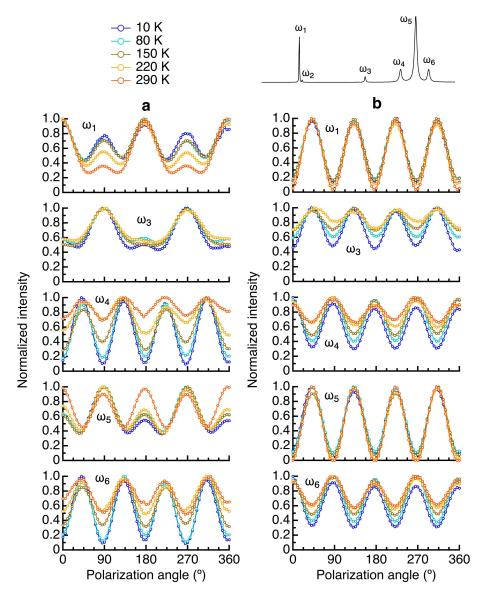


**Figure S7:** The temperature evolution of the PO dependence for the low-frequency peaks of BTBT in (a) parallel and (b) cross configurations. The intensities were normalized for each mode at each temperature.

# SIX Fitting the PO response of BTBT

# SIX.1 Data preparation and factor group analysis for BTBT

Section SVII presents the contour plots of the PO Raman measurement of BTBT at 10, 80, 150 220, and 290 K in parallel and cross configurations. The measurements were performed as described in Sec. SI. To extract the polarization dependence of the integrated intensity of each peak we fit the spectra at each polarization angle to a multi-damped Lorentz oscillator (see section SIII). The dotted lines in Figures S8 and S9 show the integrated intensity of each damped Lorentz oscillator with respect to the excitation polarization angle. Next, for the second-rank Raman tensor formalism we extract the form of the Raman tensors, as well as the expected number of lattice modes and their vibrational symmetry, by using factor group analysis with the relevant space group (monoclinic,  $P2_1/c$ ) [7]. For BTBT, factor group analysis predicts 6 Raman-active lattice libration modes, and indeed our measured spectra showed exactly six distinguishable Raman peaks.

# SIX.2 Fitting the PO with a second-rank tensor

The symmetry allowed Raman tensors for  $3A_g$  and  $3B_g$  are[8]:

$$\mathcal{R}_{A_{g}} = \begin{pmatrix} a & 0 & e \\ 0 & b & 0 \\ e & 0 & c \end{pmatrix}, \qquad \mathcal{R}_{B_{g}} = \begin{pmatrix} 0 & d & 0 \\ d & 0 & f \\ 0 & f & 0 \end{pmatrix}.$$
(S3)

We perform a global fit to the integrated intensity in both parallel and cross configurations using the second-rank Raman tensor formalism described by Eq. (1) in the main text (see Ref. [9] for more details regarding the fitting process).

Figure S8 shows the results for this fitting procedure at all measured temperatures. The 10 K fits show that  $\omega_1$ ,  $\omega_3$ , and  $\omega_5$  are  $A_g$  modes, while  $\omega_4$  and  $\omega_6$  are  $B_g$  modes. The intensity of  $\omega_2$  was too weak to extract its polarization dependence reliably. The fit gets worse for  $\omega_3$ ,  $\omega_4$  and  $\omega_6$  as temperature increases, while for  $\omega_1$  and  $\omega_5$  the fit is successful in all temperatures.

To further challenge the necessity of a fourth-rank tensor, we attempted fitting a symmetry-

relaxed second-rank tensor:

$$\tilde{\mathcal{R}} = \begin{pmatrix} a & d_1 & e_1 \\ d_2 & be^{i\delta} & f_1 \\ e_2 & f_2 & c \end{pmatrix},$$
(S4)

where we introduce a relative phase  $\delta$  to account for possible birefringence effects [10], and allow asymmetric components (effectively relaxing time-symmetry) [11]. Adapted to our back-scattering geometry,  $\tilde{\mathcal{R}}$  has five independent parameters  $(a, b, d_1, d_2, \delta)$ . As Fig. S8 demonstrates, this generalized second-rank tensor form was still unable to fit the observed PO pattern of  $\omega_4$ .

# SIX.3 Fitting the PO with a fourth-rank tensor

Applying the symmetry constraints of the relevant space group  $(P2_1/c)$  along with the intrinsic left and right minor symmetries, and retaining only the components relevant for our back-scattering geometry, the effective fourth-rank tensor used for fitting the PO patterns was:

Figure S9 shows the fit results for the same PO Raman data set by using the fourth-rank Raman tensor formalism. Here we see that the fit is excellent at all temperatures. These results are discussed in the main text.

#### SIX.4 Global fit with the two-mode model

The full PO data for spectral features  $\omega_4$  and  $\omega_5$  at 10 K was globally fitted using the two-mode model discussed in the main text, with birefringence effects incorporated as in the harmonic case of Sec. S9.2, introducing the additional parameter  $\delta$ .

In practice, this means simultaneously fitting the spectral range 85-95  $cm^{-1}$  for all 144 spectra (72 polarization angles for each polarization configuration) to:

$$\sigma(\Omega) \propto \sum_{\mu\nu\xi\rho} n_{\mu} n_{\xi} I_{\mu\nu\xi\rho}(\Omega) E_{\nu} E_{\rho}, \tag{S6}$$

with

$$I_{\mu\nu\xi\rho}(\Omega) = \left[n_{BE}(\Omega, T) + 1\right] \left[ \chi_{A_g}^{*\mu\nu} \chi_{A_g}^{\xi\rho} J_{A_gA_g} + \chi_{B_g}^{*\mu\nu} \chi_{B_g}^{\xi\rho} J_{B_gB_g} \right], \tag{S7}$$

and

$$\chi_{A_{g}} = \begin{pmatrix} a & 0 & e \\ 0 & be^{i\delta} & 0 \\ e & 0 & c \end{pmatrix}, \qquad \chi_{B_{g}} = \begin{pmatrix} 0 & de^{i\delta} & 0 \\ de^{i\delta} & 0 & fe^{i\delta} \\ 0 & fe^{i\delta} & 0 \end{pmatrix}.$$
(S8)

Applying our back-scattering geometry to Eq. (S6) gives the following final fitted expressions for parallel ( $\parallel$ ) and cross ( $\perp$ ) configurations:

$$\sigma_{\parallel} \propto J_{\rm AgAg} a^2 \cos^4(\Delta \theta) + 2J_{\rm AgAg} ab \cos(2\delta) \cos^2(\Delta \theta) \sin^2(\Delta \theta)^2 + 4J_{\rm BgBg} d^2 \cos^2(\Delta \theta) \sin^2(\Delta \theta) + J_{\rm AgAg} b^2 \sin^4(\Delta \theta), \quad (S9)$$

$$\sigma_{\perp} \propto J_{\rm AgAg} a^2 \cos^2(\Delta \theta) \sin^2(\Delta \theta)^2 + J_{\rm AgAg} b^2 \cos^2(\Delta \theta) \sin^2(\Delta \theta)^2 -$$

$$2J_{\rm BgBg} d^2 \cos^2(\Delta \theta) \sin^2(\Delta \theta) - 2J_{\rm AgAg} ab \cos(2\delta) \cos^2(\Delta \theta) \sin^2(\Delta \theta)^2 +$$

$$J_{\rm BgBg} d^2 \cos^4(\Delta \theta) + J_{\rm BgBg} d^2 \sin^4(\Delta \theta), \quad (S10)$$

where  $\Delta\theta = \theta - \theta_0$  is determined by the incident polarization  $\theta$ , controlled in experiment, and  $\theta_0$  is a global angle determined by the crystal orientation. The spectral frequency dependency is contained within the spectral functions  $J_{\lambda\lambda'}(\Omega)$  and the  $[n_{BE}(\Omega,T)+1]$  factor.

The full derivation of  $J_{\lambda\lambda'}$  for the two-mode model is given in the main text, equations (6), (7), (9). This yielded the final function used in the global fit (using the shorthand  $A_g \equiv 1$  and  $B_g \equiv 2$ ):

$$J_{11}(\Omega) = \frac{\Gamma_2 \left( -\gamma^* \gamma - \Gamma_1 \Gamma_2 + \left( \frac{\Omega^2 - \omega_1^2}{2\omega_1} \right) \left( \frac{\Omega^2 - \omega_2^2}{2\omega_2} \right) \right) - \left( \frac{\Omega^2 - \omega_2^2}{2\omega_2} \right) \left( \Gamma_1 \left( \frac{\Omega^2 - \omega_2^2}{2\omega_2} \right) + \Gamma_2 \left( \frac{\Omega^2 - \omega_1^2}{2\omega_1} \right) \right)}{\left( -\gamma^* \gamma - \Gamma_1 \Gamma_2 + \left( \frac{\Omega^2 - \omega_1^2}{2\omega_1} \right) \left( \frac{\Omega^2 - \omega_2^2}{2\omega_2} \right) \right)^2 + \left( \Gamma_1 \left( \frac{\Omega^2 - \omega_2^2}{2\omega_2} \right) + \Gamma_2 \left( \frac{\Omega^2 - \omega_1^2}{2\omega_1} \right) \right)^2}, \quad (S11)$$

with  $J_{B_gB_g}$  being the same only with swapped irrep indices  $(A_g \leftrightarrow B_g)$ .

The full list of fit parameters is therefore:

- 1.  $\omega_i$  the peak resonance
- 2.  $\Gamma_i$  the peak width
- 3.  $\theta_0$  global incident polarization off-set

The three parameters mentioned above are identical to those used to extract the integrated intensity in the harmonic analysis. They govern the peak shape, but not the PO pattern. The parameters that create the PO response in our two-mode model are:

- 4. a susceptibility derivative for  $A_g$  normal mode
- 5. b susceptibility derivative for  $A_g$  normal mode
- 6. d susceptibility derivative for  $\mathbf{B}_{\mathbf{g}}$  normal mode
- 7.  $\delta$  phase retardance due to birefringence
- 8.  $\gamma$  off-diagonal self-energy component

which gives a total of five parameters for two spectral peaks, the same as in the generalized second-rank formalism that failed to account for the PO response of the single  $\omega_4$  peak.

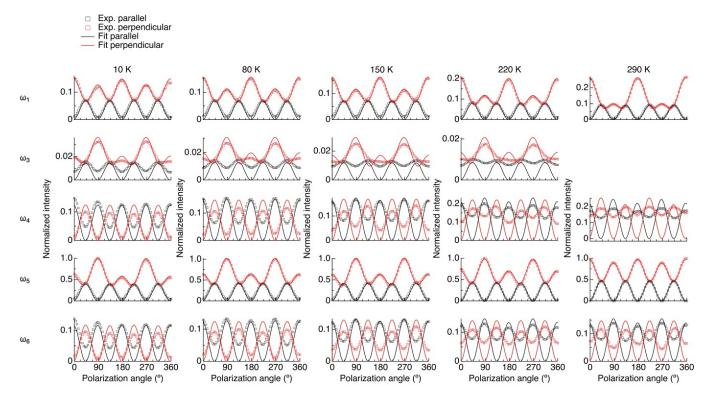


**Figure S8:** Fitting results for the PO Raman response of BTBT at different temperatures, using a general second-rank Raman tensor.

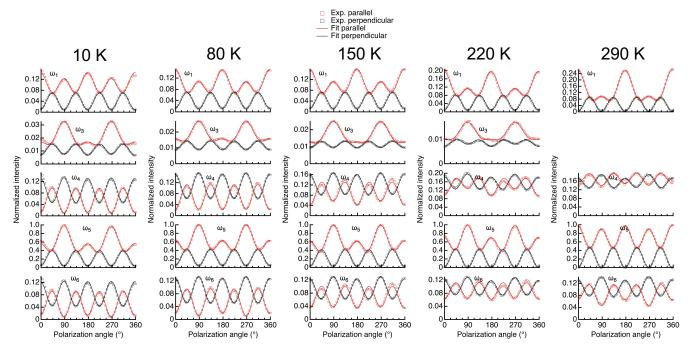


**Figure S9:** Fitting results for the PO Raman response of BTBT at different temperatures, showing the successful fit obtained by using the fourth-rank formalism.

#### SIX.5 Positive semi-definite fourth-rank tensors

Unlike the harmonic expression (Eq. (1) in main text), using the general fourth-rank tensor of Eq. (S6) can yield non-positive values. This poses no problem when used for fitting experimental data, but since scattering cross-sections can not be negative, this technically places further constraints on the general tensor form. Because our fourth-rank tensor has the same symmetry of the elastic stiffness tensor, we can apply the positive semi-definiteness constraint by adopting Voigt notation, where the tensor is re-written as a 6X6 matrix [12, 13].

We begin by defining the extended vectors  $\tilde{\boldsymbol{n}}$  and  $\tilde{\boldsymbol{E}}$ :

$$\tilde{\boldsymbol{n}} = \begin{pmatrix} n_x^2 \\ n_y^2 \\ n_z^2 \\ n_y n_z \\ n_x n_z \\ n_x n_y \end{pmatrix}; \qquad \tilde{\boldsymbol{E}} = \begin{pmatrix} E_x^2 \\ E_y^2 \\ E_z^2 \\ E_y E_z \\ E_x E_z \\ E_x E_y \end{pmatrix}. \tag{S12}$$

If we write the following 6X6 matrix in terms of the fourth-rank tensor terms:

$$\tilde{I} = \begin{pmatrix}
I_{1111} & I_{1212} & I_{1313} & 2I_{1213} & 2I_{1113} & 2I_{1112} \\
I_{1212} & I_{2222} & I_{2323} & 2I_{2223} & 2I_{1223} & 2I_{1222} \\
I_{1313} & I_{2323} & I_{3333} & 2I_{2333} & 2I_{3313} & 2I_{1323} \\
2I_{1213} & 2I_{2223} & 2I_{2333} & 2\left(I_{2233} + I_{2323}\right) & 2\left(I_{1233} + I_{1323}\right) & 2\left(I_{1223} + I_{1322}\right) \\
2I_{1113} & 2I_{1223} & 2I_{1333} & 2\left(I_{1233} + I_{1323}\right) & 2\left(I_{1133} + I_{1313}\right) & 2\left(I_{1123} + I_{1213}\right) \\
2I_{1112} & 2I_{1222} & 2I_{1323} & 2\left(I_{1223} + I_{1322}\right) & 2\left(I_{1123} + I_{1213}\right) & 2\left(I_{1122} + I_{1212}\right)
\end{pmatrix}, (S13)$$

then the expression

$$\tilde{I} = \tilde{\boldsymbol{n}} \cdot \tilde{I} \cdot \tilde{\boldsymbol{E}} = \sum_{\alpha\beta} \tilde{I}_{\alpha\beta} n_{\alpha} E_{\beta} \tag{S14}$$

is equivalent to the cross-section defined by Eq. (S6).

It is now straightforward to guarantee the positive semi-definiteness of Eq. (S14) by demanding all eigenvalues of the symmetric matrix  $\tilde{I}$  to be non-negative [14]. This will generally yield in-

tractable expressions. Even after applying the spatial symmetry constraints for BTBT ( $C_{2h}$  point group) the scattering tensor still has 14 independent variables with the Voigt-like matrix:

$$\tilde{I}_{C_{2h}} = \begin{pmatrix}
I_{1111} & I_{1212} & I_{1313} & 0 & 2I_{1113} & 0 \\
I_{1212} & I_{2222} & I_{2323} & 0 & 2I_{1223} & 0 \\
I_{1313} & I_{2323} & I_{3333} & 0 & 2I_{1333} & 0 \\
0 & 0 & 0 & 2(I_{2233} + I_{2323}) & 0 & 2(I_{1223} + I_{1322}) \\
2I_{1113} & 2I_{1223} & 2I_{1333} & 0 & 2(I_{1133} + I_{1313}) & 0 \\
0 & 0 & 0 & 2(I_{1223} + I_{1322}) & 0 & 2(I_{1122} + I_{1212})
\end{pmatrix} (S15)$$

which has complicated eigenvalues.

In the high-symmetry case of the  $O_h$  point group, however, the scattering tensor has only three independent variables and the Voigt-like matrix is

$$\tilde{I}_{O_h} = \begin{pmatrix}
a & b & b & 0 & 0 & 0 \\
b & a & b & 0 & 0 & 0 \\
b & b & a & 0 & 0 & 0 \\
0 & 0 & 0 & 2(b+c) & 0 & 0 \\
0 & 0 & 0 & 0 & 2(b+c) & 0 \\
0 & 0 & 0 & 0 & 0 & 2(b+c)
\end{pmatrix},$$
(S16)

which has only three different eigenvalues, such that the requirement for positive semi-definiteness becomes

$$a - b \ge 0;$$
  $b + c \ge 0;$   $a + 2b \ge 0.$  (S17)

#### SX Raman polarization-orientation measurements of anthracene and pentacene

The full PO Raman spectra of anthracene and pentacene crystals were measured in a similar fashion to that described in Sec. SI (see full measurement and irrep assignment details in [9]). The PO Raman spectra at 10 K for both anthracene and pentacene are presented in Fig. S10.

A procedure similar to that used in BTBT (Sec. SIII) was applied to extract the integrated intensity of each peak, and fit the PO pattern to both a second (Sec. SIX.2) and fourth-rank (Sec. SIX.3) formalism (all three crystals share the same  $C_{2h}$  point-group and tensor forms). The results are presented in figures S11 (second rank), S12 (fourth-rank) for anthracene, and figures S13 (second-rank), S14 (fourth-rank) for pentacene. In both cases the second-rank formalism fails to capture the PO of all peaks (specifically,  $\omega_2$ ,  $\omega_6$  for anthracene, and  $\omega_6$ ,  $\omega_6$ ,  $\omega_7$  for pentacene), whereas the fourth-rank formalism consistently yields a perfect fit.

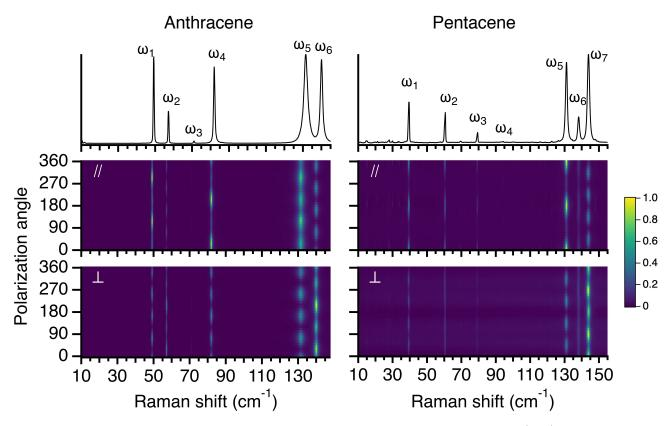


**Figure S10:** Temperature dependence of the PO Raman of anthracene (left) and pentacene (right). Top row shows the unpolarized spectra. Middle and bottom rows present the PO for parallel and cross configurations, respectively.

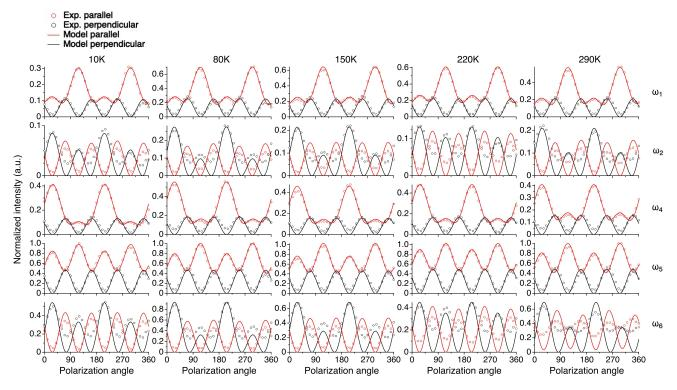


Figure S11: Fitting results for the PO Raman response of anthracene at different temperatures, using a general second-rank Raman tensor. The fit for peaks  $\omega_2$ ,  $\omega_6$  is unsatisfactory.

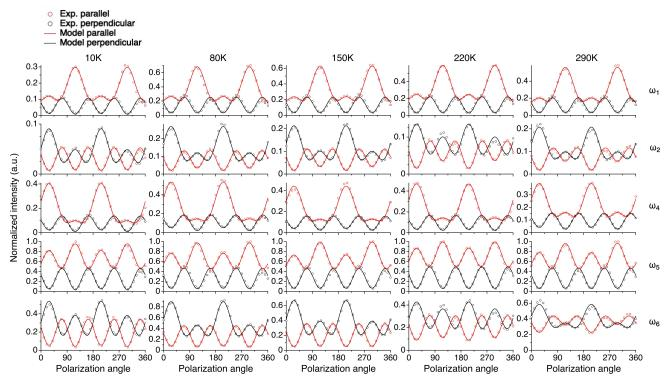


Figure S12: Fitting results for the PO Raman response of anthracene at different temperatures, showing the successful fit obtained by using the fourth-rank formalism.

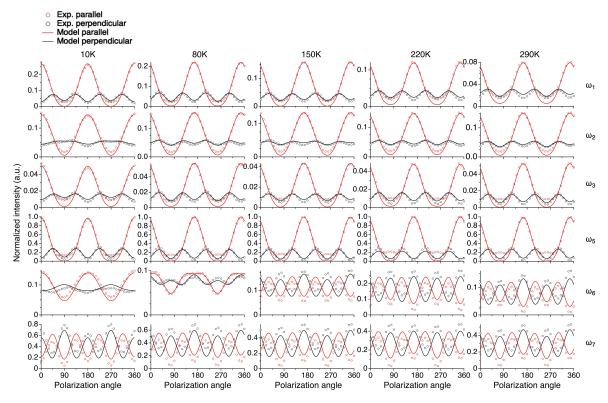


Figure S13: Fitting results for the PO Raman response of pentacene at different temperatures, using a general second-rank Raman tensor. The fit for peaks  $\omega_5$ ,  $\omega_6$ ,  $\omega_7$  is unsatisfactory.

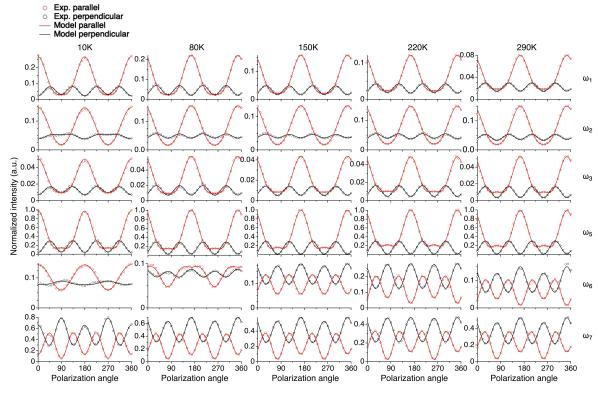


Figure S14: Fitting results for the PO Raman response of pentacene at different temperatures, showing the successful fit obtained by using the fourth-rank formalism.

# SXI Theory of inelastic light scattering from crystals at finite temperatures

# SXI.1 Vibrational excitations of an anharmonic crystal

In this section we outline the procedure to determine the Raman spectrum of an anharmonic crystal. We will begin by sketching the procedure to obtain the phonon-phonon correlation function in the presence of three-phonon anharmonicity via the equation of motion approach.

If we express the atomic displacements in terms of creation and annihilation operators we can identify the reciprocal space coefficients needed for the perturbative expansion, repeated here for clarity and consistency of notation. Start with the standard creation and annihilation operators for a phonon with momentum q and polarization s (when there is no loss of clarity we use the compound index  $\lambda$  to denote qs):

$$a_{qs} = \frac{1}{\sqrt{2N\hbar}} \sum_{i\alpha} \epsilon_{qs}^{i\alpha} \left( \sqrt{m_i \omega_{qs}} u_{i\alpha} - i \frac{p_{i\alpha}}{\sqrt{m_i \omega_{qs}}} \right) e^{-i\mathbf{q} \cdot \mathbf{r}_i}$$
 (S18)

$$a_{\mathbf{q}s}^{\dagger} = \frac{1}{\sqrt{2N\hbar}} \sum_{i\alpha} \epsilon_{\mathbf{q}s}^{i\alpha\dagger} \left( \sqrt{m_i \omega_{\mathbf{q}s}} u_{i\alpha} + i \frac{p_{i\alpha}}{\sqrt{m_i \omega_{\mathbf{q}s}}} \right) e^{i\mathbf{q}\cdot\mathbf{r}_i}$$
 (S19)

$$A_{qs} = a_{qs} + a_{\bar{q}s}^{\dagger} = \frac{2}{\sqrt{2N\hbar}} \sum_{i\alpha} \epsilon_{qs}^{i\alpha} \sqrt{m_i \omega_{qs}} u_{i\alpha} e^{-iq \cdot r_i}$$
(S20)

$$B_{qs} = a_{qs} - a_{\bar{q}s}^{\dagger} = -\frac{2i}{\sqrt{2N\hbar}} \sum_{i\alpha} \epsilon_{qs}^{i\alpha} \frac{p_{i\alpha}}{\sqrt{m_i \omega_{qs}}} e^{-iq \cdot r_i}$$
(S21)

Here  $\epsilon$  are phonon eigenvectors ( $\epsilon_i \cdot \epsilon_j = \delta_{ij}$ ), m atomic masses and  $\omega$  frequencies. The vector  $\mathbf{r}$  is a lattice vector, and u and p are the position and momentum operators. We use the notation  $\bar{q} = -\mathbf{q}$ . We introduce scaled eigenvectors (to simplify notation) via

$$v_{\mathbf{q}s}^{i\alpha} = \sqrt{\frac{\hbar}{2m_i \omega_{\mathbf{q}s}}} \epsilon_{\mathbf{q}s}^{i\alpha} \tag{S22}$$

In this notation the matrix elements pertaining to anharmonicity become

$$\Phi_{\lambda\lambda'\lambda''} = \frac{1}{3!} \sum_{ijk\alpha\beta\gamma} \upsilon_{\mathbf{q}s}^{i\alpha} \upsilon_{\mathbf{q}'s'}^{j\beta} \upsilon_{\mathbf{q}''s''}^{k\gamma} \Phi_{ijk}^{\alpha\beta\gamma} e^{-i(\mathbf{q}\cdot\mathbf{r}_i + \mathbf{q}'\cdot\mathbf{r}_j + \mathbf{q}''\cdot\mathbf{r}_k)}$$
(S23)

$$\Phi_{\lambda\lambda'\lambda''\lambda'''} = \frac{1}{4!} \sum_{ijkl\alpha\beta\gamma\delta} \upsilon_{\mathbf{q}s}^{i\alpha} \upsilon_{\mathbf{q}'s'}^{j\beta} \upsilon_{\mathbf{q}''s''}^{k\gamma} \upsilon_{\mathbf{q}'''s'''}^{l\delta} \Phi_{ijkl}^{\alpha\beta\gamma\delta} e^{-i(\mathbf{q}\cdot\mathbf{r}_i + \mathbf{q}'\cdot\mathbf{r}_j + \mathbf{q}''\cdot\mathbf{r}_k + \mathbf{q}'''\cdot\mathbf{r}_l)}$$
(S24)

so that the anharmonic part of the Hamiltonian becomes

$$H_A = \Phi_{\lambda \lambda' \lambda''} A_{\lambda} A_{\lambda'} A_{\lambda''} + \Phi_{\lambda \lambda' \lambda'' \lambda'''} A_{\lambda} A_{\lambda'} A_{\lambda''} A_{\lambda'''} + \cdots$$
 (S25)

In an analogous way we define the coefficients of the expansion of the polarizability as

$$\chi_{\lambda}^{\mu\nu} = \sum_{i\alpha} v_{\mathbf{q}s}^{i\alpha} \chi_i^{\mu\nu,\alpha} e^{-i\mathbf{q}\cdot\mathbf{r}_i} \Delta_{\mathbf{q}} = \sum_{i\alpha} v_{\Gamma s}^{i\alpha} \chi_i^{\mu\nu,\alpha} = \chi^{\mu\nu}(s)$$
 (S26)

$$\chi_{\lambda\lambda'}^{\mu\nu} = \frac{1}{2!} \sum_{ij\alpha\beta} v_{\mathbf{q}s}^{i\alpha} v_{\mathbf{q}'s'}^{j\beta} \chi_{ij}^{\mu\nu,\alpha\beta} e^{-i\mathbf{q}\cdot\mathbf{r}_i} e^{-i\mathbf{q}'\cdot\mathbf{r}_j} \Delta_{\mathbf{q}\mathbf{q}'}$$
(S27)

$$= \frac{1}{2!} \sum_{ij\alpha\beta} v_{\mathbf{q}s}^{i\alpha} (v_{\mathbf{q}s'}^{j\beta})^{\dagger} \chi_{ij}^{\mu\nu,\alpha\beta} e^{i\mathbf{q}\cdot(\mathbf{r}_j - \mathbf{r}_i)}$$
(S28)

$$= \frac{1}{2!} \sum_{ij\alpha\beta} (v_{\boldsymbol{q}s}^{i\alpha})^{\dagger} v_{\boldsymbol{q}s'}^{j\beta} \chi_{ij}^{\mu\nu,\alpha\beta} e^{-i\boldsymbol{q}\cdot(\boldsymbol{r}_j - \boldsymbol{r}_i)} = \chi^{\mu\nu}(\boldsymbol{q}, s, s') = \chi^{\mu\nu}(\bar{\boldsymbol{q}}, s, s')^{\dagger} = \chi^{\mu\nu}(\bar{\boldsymbol{q}}, s', s) \qquad (S29)$$

$$\chi_{\lambda\lambda'\lambda''}^{\mu\nu} = \frac{1}{3!} \sum_{ijk\alpha\beta\gamma} v_{\mathbf{q}'s'}^{i\alpha} v_{\mathbf{q}'s'}^{j\beta} \chi_{ijk}^{k\gamma} \chi_{ijk}^{\mu\nu,\alpha\beta\gamma} e^{-i(\mathbf{q}\cdot\mathbf{r}_i + \mathbf{q}'\cdot\mathbf{r}_j + \mathbf{q}''\cdot\mathbf{r}_k)}$$
(S30)

Such that

$$\chi^{\mu\nu} = \chi_0^{\mu\nu} + \chi_{\lambda}^{\mu\nu} A_{\lambda} + \chi_{\lambda\lambda'}^{\mu\nu} A_{\lambda} A_{\lambda'} + \chi_{\lambda\lambda'\lambda''}^{\mu\nu} A_{\lambda} A_{\lambda'} A_{\lambda''} + \cdots$$
 (S31)

#### SXI.2 Raman scattering in terms of the anharmonic Green's function

If we start from the polarizability-polarizability correlation function and insert the expansion of the polarizability in terms of phonon coordinates, Eq. (S31), we get

$$\langle \chi(t)\chi(0)\rangle = \chi_{0} \otimes \chi_{0} + \chi_{\lambda} \otimes \chi_{\lambda'}i\overset{>}{G}(A_{\lambda}, A_{\lambda'}) +$$

$$+ \chi_{\lambda\lambda'} \otimes \chi_{\lambda''\lambda'''}i\overset{>}{G}(A_{\lambda}A_{\lambda'}, A_{\lambda'''}A_{\lambda'''}) +$$

$$+ \chi_{\lambda} \otimes \chi_{\lambda'\lambda''}i\overset{>}{G}(A_{\lambda}, A_{\lambda'}A_{\lambda''}) + \chi_{\lambda\lambda'} \otimes \chi_{\lambda''}i\overset{>}{G}(A_{\lambda}A_{\lambda'}, A_{\lambda''}) +$$

$$+ \chi_{\lambda} \otimes \chi_{\lambda'\lambda''\lambda'''}i\overset{>}{G}(A_{\lambda}, A_{\lambda'}A_{\lambda''}A_{\lambda'''}) + \chi_{\lambda\lambda'\lambda''} \otimes \chi_{\lambda'''}i\overset{>}{G}(A_{\lambda}A_{\lambda'}A_{\lambda''}, A_{\lambda'''}),$$
(S32)

where  $\overset{>}{G}(A_{\lambda},A_{\lambda'}^{\dagger},\tau) \equiv -i\langle A_{\lambda}(\tau),A_{\lambda'}(0)\rangle$ , and we have omitted terms of  $A^4$  or higher. The physical quantity of interest here is the spectral function,  $J_{\lambda\lambda'}(\Omega)$ , which may also be written in terms of

the retarded Green's function,  $G_{\lambda\lambda'}^R(\Omega,T) = -i\int \theta(\tau) \left\langle \left[ A_{\lambda}(\tau), A_{\lambda'}^{\dagger}(0) \right] \right\rangle_T e^{-i\Omega t} dt$ 

$$J_{\lambda\lambda'}(\Omega) = -\frac{1}{\pi} \operatorname{Im} \left\{ G_{\lambda\lambda'}^{R}(\Omega) \right\} = \frac{i}{(n(\Omega, T) + 1)} \stackrel{>}{G}_{\lambda\lambda'}(\Omega), \tag{S33}$$

where  $n(\Omega, T)$  is the Bose-Einstein occupation number for energy  $\hbar\Omega$  at temperature T, and with the retarded Green's function conveniently given in terms of the sum of a diagonal harmonic part,  $g_{\lambda\lambda'}^0(\Omega)$ , and the self-energy term  $\Sigma_{\lambda\lambda'}(\Omega)$ :

$$G^{R}(\Omega)^{-1} = g^{0}(\Omega)^{-1} + \Sigma(\Omega). \tag{S34}$$

Following the work of others [15–18], we have previously discussed in detail the solution for the retarded Green's function of an anharmonic system  $H_A$  [19]. In the case of third-order anharmonicity, the self-energy is given by

$$\Sigma_{\lambda\lambda'}(\Omega) = -18 \sum_{q_1 q_2 s_1 s_2} \Phi_{q\bar{q}_1 \bar{q}_2}^{\lambda s_1 s_2} \Phi_{\bar{q} q_1 q_2}^{\lambda' s_1 s_2} S(s_1, s_2, \Omega)$$
 (S35)

and

$$S(s_a, s_b, \Omega) = (n_a + n_b + 1) \left[ \frac{1}{(\omega_a + \omega_b - \Omega)_p} - \frac{1}{(\omega_a + \omega_b + \Omega)_p} \right] + (n_a - n_b) \left[ \frac{1}{(\omega_b - \omega_a + \Omega)_p} - \frac{1}{(\omega_b - \omega_a - \Omega)_p} \right].$$
(S36)

The constant (zeroth) term in Eq. (S32) does not contribute to the Raman spectrum. Using the spectral function (S33), the first term becomes

$$I^{\mathrm{I}} = \chi_{\lambda} \otimes \chi_{\lambda'} \int i \overset{>}{G} (A_{\lambda}(t), A_{\lambda'}(0)) e^{-i\Omega t} dt = \chi_{\lambda} \otimes \chi_{\lambda'}(n(\Omega) + 1) J_{\lambda\lambda'}(\Omega).$$
 (S37)

This is sufficient to understand the origin of the polarization dependence presented in this study. Higher terms in expansion (S32) are usually smaller, but become significant in Raman inactive structures, where the derivatives in Eq. (S37) identically vanish. This will happen for any crystal where all atomic sites constitute a center of inversion. See [19] for a detailed discussion for the case of rock-salt structure, as well as how higher-order terms might play a role in finite temperatures.

# SXI.3 Light scattering in harmonic systems

In harmonic systems all inter-atomic interactions are reduced to terms quadratic in their displacement from equilibrium in the potential expansion [20]. These produce ideal, non-interacting normal mode solutions,  $G_{\lambda\lambda'}(\Omega) = g_{\lambda\lambda}^0(\Omega)\delta_{\lambda\lambda'}$  [16]. Using the harmonic spectral function [21], the Stokes component in Eq. (S37) becomes

$$I(\Omega, T) = \sum_{\lambda} \chi_{\lambda}^* \otimes \chi_{\lambda} \frac{[n(\Omega, T) + 1]}{2\omega_{\lambda}} \delta(\Omega - \omega_{\lambda}).$$
 (S38)

The inadequacy of a purely harmonic treatment in light scattering is already partially recognized in most Raman studies, at least implicitly. As Eq. (S38) shows, the frequency dependence of a truly harmonic system should be a delta-function. In practice, a Lorentzian-like line shape is commonly used, and explained by the same spectral function  $J(\Omega)$ , or more explicitly  $(\text{Im}\{\Sigma_{\lambda\lambda}\})^{-1}$ , commonly known as the phonon lifetime [22]. In addition, thermal expansion is sometimes incorporated through a quasi-harmonic treatment where the normal modes become volume dependent [23].

If only diagonal terms are considered (note that the self-energy need not vanish for this), the generalized fourth-rank expression of Eq. (S6) reduces back to the temperature *independent* PO response (Eq. (1) in main text), and all PO patterns may be explained in terms of a single second-rank tensor  $\mathcal{R}$ . This is demonstrated by plugging Eq. (S38) into Eq. (S6). The incident field,  $\mathbf{E}_i$ , observed scattering polarization,  $\mathbf{n}$ , and second-rank tensor,  $\chi_{\lambda}$  are defined as:

$$\boldsymbol{E}_{i} = |\boldsymbol{E}_{i}| \begin{pmatrix} e_{x} \\ e_{y} \\ e_{z} \end{pmatrix}; \qquad \boldsymbol{n} \equiv \hat{\boldsymbol{e}}_{s} = \begin{pmatrix} n_{x} \\ n_{y} \\ n_{z} \end{pmatrix}; \qquad \mathcal{R} \equiv \boldsymbol{\chi}_{\lambda} = \begin{pmatrix} \chi_{xx} & \chi_{xy} & \chi_{xz} \\ \chi_{yx} & \chi_{yy} & \chi_{yz} \\ \chi_{zx} & \chi_{zy} & \chi_{zz} \end{pmatrix}. \tag{S39}$$

The polarization dependence of the scattering cross-section for a single mode  $\lambda$  becomes:

$$\sigma \propto \sum_{\mu\nu\xi\rho} n_{\mu}n_{\xi}I_{\mu\nu,\xi\rho}E_{\nu}E_{\rho}$$

$$= \left[n(\omega_{\lambda},T)+1\right] \frac{|E_{i}|^{2}}{2\omega_{\lambda}} \sum_{\mu\nu\xi\rho} n_{\mu}n_{\xi} \left(\boldsymbol{\chi}_{\lambda}^{*} \otimes \boldsymbol{\chi}_{\lambda}\right)_{\mu\nu\xi\rho} e_{\nu}e_{\rho}$$

$$\propto \sum_{\mu\nu\xi\rho} n_{\mu}n_{\xi}\boldsymbol{\chi}_{\nu\mu}^{*}\boldsymbol{\chi}_{\rho\xi}e_{\nu}e_{\rho}$$

$$= \left(\sum_{\nu\mu} \boldsymbol{\chi}_{\nu\mu}^{*}n_{\mu}e_{\nu}\right) \left(\sum_{\rho\xi} \boldsymbol{\chi}_{\rho\xi}n_{\xi}e_{\rho}\right) = \left(\sum_{\nu\mu} \boldsymbol{\chi}_{\nu\mu}n_{\mu}e_{\nu}\right)^{*} \left(\sum_{\rho\xi} \boldsymbol{\chi}_{\rho\xi}n_{\xi}e_{\rho}\right)$$

$$= \left|\sum_{ij} \boldsymbol{\chi}_{ij}n_{j}e_{i}\right|^{2} = \left|\sum_{i} e_{i} \sum_{j} \boldsymbol{\chi}_{ij}n_{j}\right|^{2}$$

$$= |\hat{e}_{i} \cdot \mathcal{R} \cdot \hat{e}_{s}|^{2},$$

which is exactly the original second-rank expression.

#### References

- (1) Vyas, V. S.; Gutzler, R.; Nuss, J.; Kern, K.; Lotsch, B. V. CrystEngComm **2014**, 16, 7389–7392.
- (2) Niebel, C. et al. Journal of Materials Chemistry C 2015, 3, 674–685.
- (3) Matsumura, M.; Muranaka, A.; Kurihara, R.; Kanai, M.; Yoshida, K.; Kakusawa, N.; Hashizume, D.; Uchiyama, M.; Yasuike, S. *Tetrahedron* **2016**, *72*, 8085–8090.
- (4) Macrae, C. F.; Bruno, I. J.; Chisholm, J. A.; Edgington, P. R.; McCabe, P.; Pidcock, E.; Rodriguez-Monge, L.; Taylor, R.; Van De Streek, J.; Wood, P. A. Journal of Applied Crystallography 2008, 41, 466–470.
- Macrae, C. F.; Edgington, P. R.; McCabe, P.; Pidcock, E.; Shields, G. P.; Taylor, R.; Towler,
   M.; Van De Streek, J. Journal of Applied Crystallography 2006, 39, 453–457.
- (6) Lu, Z. Q.; Quinn, T; Reehal, H. S. Journal of Applied Physics 2005, 97, 033512.
- (7) Rousseau, D. L.; Bauman, R. P.; Porto, S. P. S. Journal of Raman Spectroscopy 1981, 10, 253–290.
- (8) Aroyo, M. I.; Perez-Mato, J. M.; Capillas, C.; Kroumova, E.; Ivantchev, S.; Madariaga, G.; Kirov, A.; Wondratschek, H. Zeitschrift für Kristallographie Crystalline Materials 2006, 221, 15–27.
- (9) Asher, M.; Angerer, D.; Korobko, R.; Diskin-Posner, Y.; Egger, D. A.; Yaffe, O. Advanced Materials 2020, 32, 1908028.
- (10) Kranert, C.; Sturm, C.; Schmidt-Grund, R.; Grundmann, M. Physical Review Letters 2016, 116, 127401.
- (11) Yu, P. Y.; Cardona, M., Fundamentals of Semiconductors; Graduate Texts in Physics, Vol. 1; Springer Berlin Heidelberg: Berlin, Heidelberg, 2010.
- (12) Nye, J.; Nye, P., Physical Properties of Crystals: Their Representation by Tensors and Matrices; Oxford science publications; Clarendon Press: 1985.
- (13) Slezák, O.; Lucianetti, A.; Mocek, T. J. Opt. Soc. Am. B 2020, 37, 1090–1097.

- (14) Van den Bos, A. In *Parameter Estimation for Scientists and Engineers*; John Wiley & Sons, Inc.: Hoboken, NJ, USA, 2007, pp 259–263.
- (15) Leibfried, G.; Ludwig, W. Solid State Physics Advances in Research and Applications 1961, 12, 275–444.
- (16) Cowley, R. Advances in Physics 1963, 12, 421–480.
- (17) Wallace, D. C., *Thermodynamics of crystals*; Dover Books on Physics; Dover Publications, Incorporated: 1998.
- (18) Semwal, B. S.; Sharma, P. K. Physical Review B 1972, 5, 3909–3914.
- (19) Benshalom, N.; Reuveni, G.; Korobko, R.; Yaffe, O.; Hellman, O. *Physical Review Materials* **2022**, *6*, 033607.
- (20) Dove, M., Structure and Dynamics: An Atomic View of Materials, 1st; Oxford University Press Inc.: New-York, 2003, p 334.
- (21) Kwok, P. C. K. In Seitz, F., Turnbull, D., Ehrenreich, H. B. T. S. S. P., Eds.; Academic Press: 1968; Vol. 20, pp 213–303.
- (22) Maradudin, A. A.; Fein, A. E.; Vineyard, G. H. *Physica Status Solidi (B)* **1962**, *2*, 1479–1492.
- (23) Fultz, B. *Progress in Materials Science* **2010**, *55*, 247–352.